Enhanced Technique for Accurate Localization and Life-Sign Detection of Human Subjects Using Beam-Steering Radar Architectures

Marco Mercuri, *Senior Member, IEEE*, Giulia Sacco, *Member, IEEE*, Rainer Hornung, Huib Visser, *Senior Member, IEEE*, Ilde Lorato, Stefano Pisa, *Senior Member, IEEE*, Pierangelo Veltri, *Member, IEEE*, and Guido Dolmans, *Senior Member, IEEE*

***Abstract*—In this work, we propose a signal processing technique for beam-steering radar architectures allowing concurrent two-dimensional (2-D) localization and vital signs monitoring of human subjects. We demonstrated it by using a single-input single-output (SISO) frequency-modulated continuous wave (FMCW) radar which integrates two frequency-scanning antennas (FSAs). This method is capable of isolating the Doppler signal generated by each single subject from the contributions of all the reflections in the monitored environment. This allows determining the number of individuals in the room and accurately measuring their vital signs parameters (respiration and heart rates) and 2-D positions (range and azimuth information). The spectral analysis, the data matrix generation and the signal processing technique are detailed and discussed. Experimental results demonstrated the feasibility of the proposed approach, showing the ability in determining the number of subjects present in the room, in accurately measuring and tracking over time their vital signs parameters, and in 2-D localization with errors within the limits of the radar range and angular resolutions. Practical applications arise for healthcare, Hospital 4.0, Internet of Medical Things (IoMT), ambient assisted living, smart buildings and through-wall sensing.**

***Index Terms*—2-D localization, beam-steering radars, health monitoring, radar-based physiological measurement techniques, radar signal processing, remote people monitoring, single-input and single-output radar, vital signs monitoring.**

Manuscript received 1 July 2024; revised 26 August 2024; accepted 14 September 2024. Date of publication 18 September 2024; date of current version 22 January 2025. This work was supported in part by the LoLiPoP-IoT Project (HORIZON-KDT-JU-2022-2-RIA) under Grant 101112286, in part by the DistriMuSe Project (HORIZON-KDT-JU-2023-2-RIA) under Grant 101139769, and in part by the European Union's Horizon Europe Research and Innovation Program through the Marie Skłodowska-Curie IN-SIGHT under Project N°101063966. *(Corresponding author: Marco Mercuri.)*

Marco Mercuri is with the Dipartimento Ingegneria dell'Informazione, delle Infrastrutture e dell'Energia Sostenibile (DIIES), University Mediterranea of Reggio Calabria, 89124 Reggio Calabria, Italy (e-mail: marco.mercuri@unirc.it).

Giulia Sacco is with the Institut d'É lectronique et des Technologies du nume´Rique (IETR), University of Rennes, UMR CNRS 6164, France.

Rainer Hornung, Huib Visser, Ilde Lorato, and Guido Dolmans are with the imec-Netherlands, The Netherlands.

Stefano Pisa is with the Department of Information Engineering Electronics and Telecommunication of Sapienza University of Rome, Italy.

Pierangelo Veltri is with the Dipartimento di Informatica, Modellistica, Elettronica e Sistemistica (DIMES), University of Calabria, Italy.

Digital Object Identifier 10.1109/TBME.2024.3463199

I. Introduction

OVER the last two decades, radar technology has been significantly investigated as a reliable solution for remote people monitoring, providing benefits of long-term vital signs monitoring (measure of respiration and heart rates), diagnosis (e.g., detection of sleep apnea syndrome, arrhythmias, ...), and prompt detection of emergencies (e.g., heart attacks, fall detection). All this without raising privacy concerns and side health effects [1], [2], [3], [4], [5].

Significant efforts have been done at circuit and system level to develop low-cost, miniaturized, high detection sensitivity and large-range motion-detection radars [6], [7], [8], [9], [10], [11], [12], [13], [14], [15], [16], [17], [18]. The first investigated devices were based on the continuous wave (CW) signals [6], [7], [8], [9], [10], [11], [12], [13], [14], [15], [16], [17], [18]. In this category fall architectures like the traditional homodyne/heterodyne [6], [7], [8], [9], [10], [11], [12], [13], the self/mutual- injection locking [14], [15], [16], and the frequency-/phase- tracking [17], [18]. However, due to their narrowband nature, these solutions can monitor only the vital signs and speed information of a single subject, without providing any information on their location. To overcome this limitation, the attention has been focused on ultra-wideband (UWB) radars that are based on frequency-modulated continuous wave (FMCW), stepped-frequency continuous wave (SFCW), phase-modulated continuous wave (PMCW), UWB impulse-radio (UWB-IR) architectures [19], [20], [21], [22], [23], [24], [25], [26], [27], [28], [29], [30], [31], [32], [33], [34], [35], [36], [37], [38], [39], [40], [41], [42], [43], [44], [45], [46], [47], [48], [49], [50], [51], [52], [53], [54]. Single-input and single-output (SISO) UWB radars have been initially proposed to continuously locate multiple people while detecting their vital signs parameters and speed profiles [19], [20], [21], [22], [23], [24], [25], [26], [27], [28], [29], [30], [31], [32], [33], [34], [35], [36], [37], [38], [39]. However, conventional SISO architectures cannot provide azimuth information and hence they cannot resolve targets which are at the same absolute distances from the radar.

The most investigated solutions for two-dimensional (2-D) localization (potentially also 3-D), vital signs, and speed detection are based on multiple-input and multiple-output (MIMO) and beam-scanning architectures [40], [41], [42], [43], [44], [45], [46], [47], [48], [49], [50], [51], [52], [53], [54]. With the capability of dividing the monitoring environment in range-angular cells, those architectures allow also mitigating the effects of the multipath propagation. This capability is even more effective with the beam-scanning architectures, where a directive beam covers only a portion of the space a time. On the contrary, with MIMO architecture, several antenna elements illuminates with quasi omnidirectional beams the room (the digital beamforming is applied only in post-processing). Electronic beam steering can be accomplished either by switching the antenna elements or by changing the relative phases of the radar signals driving the elements [51], [52], [53]. Instead, mechanical beam steering is realized involving an antenna rotation system [54]. As drawbacks, the beam steering architecture requires both several radar waveforms to be transmitted and a fast scan to cover the whole room and to aim at the targets such that their Doppler signals can be extracted satisfying the Nyquist theorem. To overcome those drawbacks, the Authors proposed the use of a SISO FMCW radar integrating two frequency-scanning antennas (FSAs) [55], [56]. The advantage is that with only two radar waveforms a whole room can be monitored. This results in a reduction of the radar range resolution, which is not necessarily a problem in people monitoring applications. Another advantage of a radar based on FSAs is that the angular resolution can be increased without adding complexity to the system. This can be achieved by optimizing the number of periods of the antenna as well as acting on the attenuation constant. This results in a more directive antenna beamwidth. On the other hand, in the case of MIMO and electronic beam steering architectures, the angular resolution can be improved by increasing the number of antennas of the array. This has as consequence a significant increase in system complexity. More precisely, MIMO radars require a higher number of radiators and consequently a higher number of transmitters and receivers. This involves higher power consumption, larger silicon's area, complex design and control, and higher amount of data to be processed. Similar drawbacks are experienced by electrical beam-steering radar sensors which would require a higher number of antennas of the arrays and consequently a higher number of time-delay and/or phase shifter units to steer the beam in the desired direction.

In parallel to the development of the radar architectures, advanced signal processing algorithms have been proposed to extract and elaborate the very weak vital signs signatures [57], [58], [59], [60]. Initial research focused on a single subject. However, to enable practical applications, multi-people monitoring has become the new research direction. One of the most investigated application is to locate and monitor the vital signs parameters of seated/lying down subjects. In most works reported in the literature, the vital signs extraction is performed knowing *a priori* the number of subjects (this information is not always available in practical applications) and sometimes their positions. Other solutions detect the variations of the range spectrum to differentiate humans from stationary targets [29], [54]. The principle is that the physiological movements involve over time a larger standard deviation (std) than static objects. However, this approach may fail when a subject is far from the radar (the std variations become smaller as the path loss increases with the distance, hence it can be overwhelmed by the noise) and in presence of multipath reflections.

In this work, we propose an alternative technique which is able to determine the number of subjects in the room and to perform concurrent vital signs monitoring and 2-D localization of seated subjects. It aims at detecting the Doppler information of each subject, isolating it from the contributions of the other reflections. Although demonstrated using an FMCW radar integrating two FSAs, this method is valid for any beam-scanning architecture. We specify that this work differentiate from our previous art [55], [56]. In [55], we proposed an FMCW radar integrating two FSAs for vital sign monitoring and 2-D localization of seated subjects, utilizing a processing algorithm based on the aforementioned std-based approach as used in [29], [54] and requiring the prior information on the number of subjects present in the room. Although the system was able to measure accurately the vital signs parameters and to properly locate the subjects, the big limitation is that it requires the prior information on the number of subjects present in the room. Moreover, it may fail in case of subjects quite separated in range (e.g., couple of meters). In [56], we proposed an FSA-based FMCW radar for 2-D indoor tracking of walking subjects. The tracking algorithm is still based on the std-based approach, hence presenting the same limitations of [29], [54], [55]. We specify that the algorithm of [56] is not able to measure the vital signs parameters. Moreover, in [56], the localization is based on detecting the curvilinear motion of the walking body while, in the proposed work, the localization of the seated subject is performed by determining the azimuth-range cell in which the periodic motion of the cardiopulmonary activity is sensed. In literature, radars integrating FSAs have been proposed as proof-of-concept in surveillance and for profile reconstruction of metallic objects (e.g., detection of concealed weapons and buried objects) and of indoor scenarios (e.g., a kitchen entrance area) [61], [62], [63], [64], [65]. To our best knowledge, those systems have never been used for remote people monitoring, which requires different signal processing approaches since the vital signs give rise to subtle phase modulations in the reflected radar signals.

The article is organized as follows. In Section II, we describe the radar's operation principle, the signal model, the creation of the data matrix and the signal processing technique. We present the radar system architecture in Section III and discuss the experimental results in Section IV.

II. Methods

A. Operational Principle and Signal Model

Fig. 1(a) shows the simplified block diagram of an FMCW radar integrating two identical FSAs, one serving as transmitter (TX) while the other as receiver (RX). The radar unit, depicted in green, consists of the source of the FMCW signals (called *chirps*), a low-noise amplifier (LNA), a mixer, an analog-to-digital converter (ADC) and four switches (SWs). The antennas

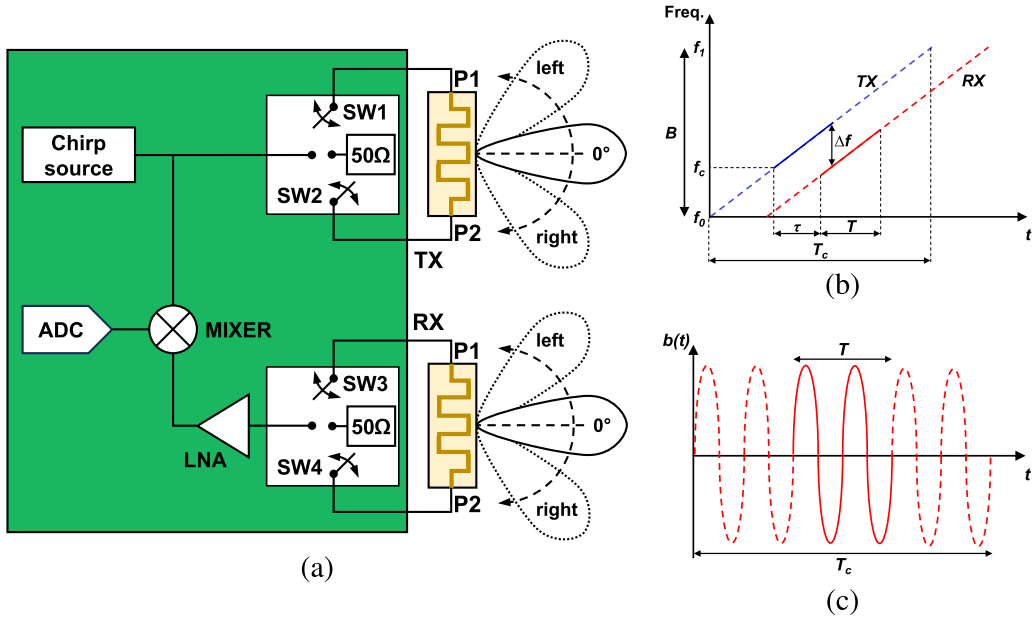

Fig. 1. Operational principle of an FMCW radar based on FSA. (a) Block diagram. (b) Frequency vs. time plot of the TX and RX *chirps*. (c) Baseband signals after mixing. The solid lines refer to an FMCW integrating FSAs while, the dashed lines, refer to non-scanning antennas.

are microstrip frequency-scanning radiators, designed to work in the same frequency range of the *chirp* (7.3–8.3 GHz), whose main beams directions can be controlled by opportunely feeding and loading the antennas. For major details on the design of an FSA, we refer the reader to [66]. Let's first consider the TX antenna. When port P1 is connected to the *chirp*'s source through the switch SW1 and the port P2 is loaded with 50 Ω, the antenna' beam points to 0° at the lowest frequency of the TX *chirp* and rotates to the right (i.e., clockwise) while increasing the frequency of the *chirp*. Reversing the feed and the load, namely connecting port P2 to the *chirp*'s source through the switch SW2 and the port P1 to the 50 Ω load, the beam rotated from 0° to the left (i.e., counterclockwise). The same consideration can be made with the RX antenna. When P1 is connected to the LNA and P2 to 50 Ω respectively through SW3 and SW4, the beam rotate from 0° to the right while receiving the reflected *chirps*. Even in this case, by reversing the feed and the load, the beam rotates to the left. Since for indoor distances, the TX and RX chirps are delayed of few nanoseconds, they can be considered to be transmitted and received essentially at the same time. Hence, the beams of the two antennas point each time to the same direction. Therefore, in far field the two beams focus simultaneously on the same target. In a normal operating condition, the beams are continuously alternated to cover both angular sectors. More precisely, when the first *chip* is transmitted and received, the feeding and load are set to cover the right angular sector. On the other hand, when the second *chip* is transmitted and received, the feeding and load are reversed to cover the left sector. These operations are continuously alternated per each *chirp*.

Fig. 1(b) compares the frequency vs. time trends of the TX and RX *chirps* for a linear FMCW radar integrating two classic antennas (dashed lines) and two FSAs (solid lines). In the first case, the duration of each signal is T_c seconds and the total bandwidth B is defined by the lowest f_0 and maximum f_1 *chirp*'s frequencies. The round-trip delay τ (of few nanoseconds and $\ll T_c$) between the TX and RX *chirps* is proportional to the nominal distance between the radar and the target. It is also proportional to the frequency shift Δf between the TX and RX *chirps*. Since with the FSAs the main beam scans while the *chirps* are transmitted/received, a target (of a finite size) is intercept by the electromagnetic (EM) signal only for a duration $T<T_c$. This also means that the effective total bandwidth $\overline{B}$ is minor of B, with initial frequency f_c. Therefore, the information corresponding to a certain target is encoded in the baseband signals, obtained mixing the TX and RX *chirps*, only for the portion of time T during which the TX and RX beams focus on the target itself (Fig. 1(c)). For major details on the FMCW radar theory, we refer the reader to [30].

Let's consider a scenario with normally breathing subjects. In the following analysis, we adopt the multipath channel model proposed by Jakes [67] and we assume valid the *stationary target assumption*, namely T_c is several order shorter than the typical cardiopulmonary period. During the interval T and for each angular sector (i.e., left or right), the digitized baseband signals can be expressed as

$$b(m,n) = \sum_i \sum_l A_{i,l}(mt_s) \cdot \sin\left[2\pi\left(\frac{\overline{B}}{T}\frac{2d_{i,l}(mt_s)}{c}nt_f + f_c\frac{2d_{i,l}(mt_s)}{c}\right)\right], \quad (1)$$

where i is the index corresponding to the i-th target/object, l is the propagation along the l-th path, $A_{i,l}$ is a complex number taking into account the overall attenuation and phase shift of the

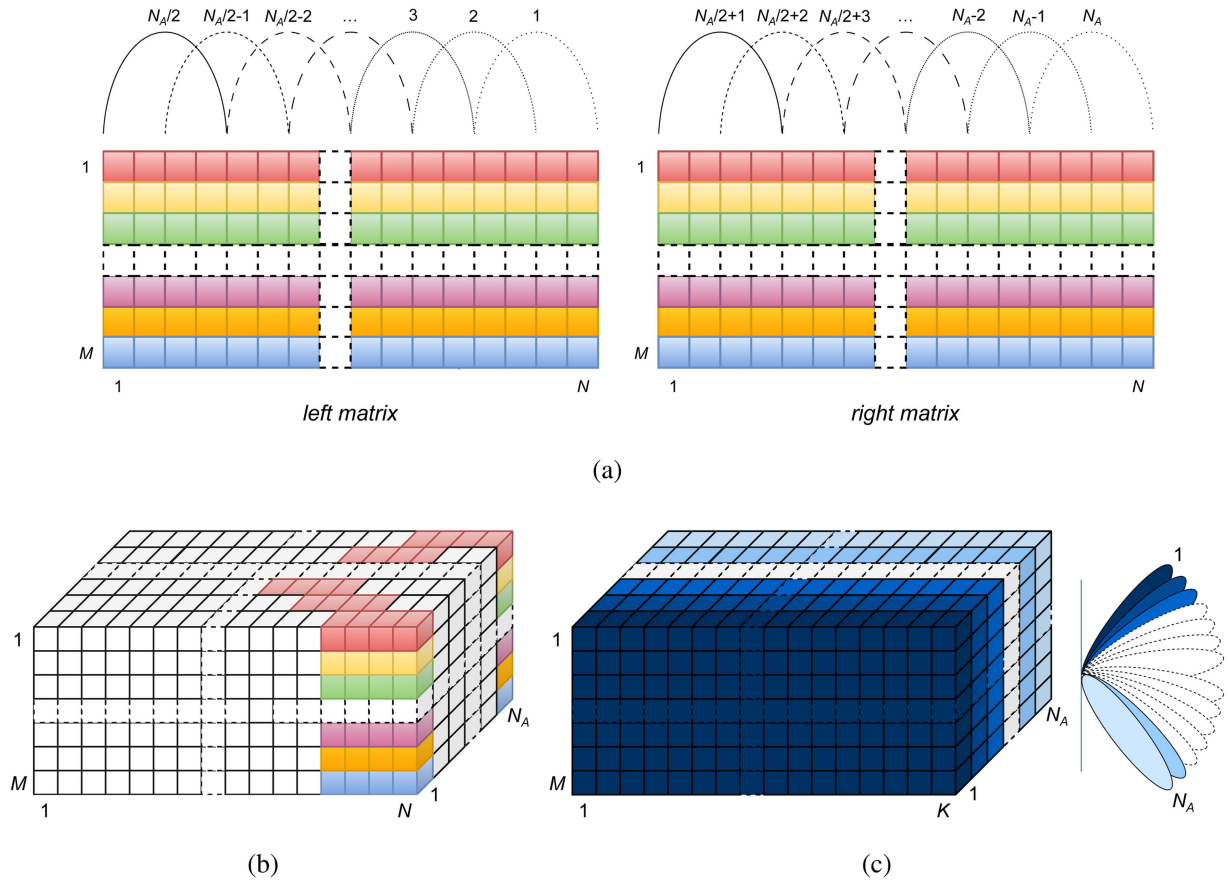

Fig. 2. Data matrix generation. (a) Windowing operation, indicated by the concave parabolas. (b) *Fast time-slow time* data matrix and zero padding operation (the solid white elements are zeros). (c) Angular-ranging matrix.

chirp during the TX and RX path and the mixing operation, $n = 1,\ldots, N$ and $m = 1,\ldots, M$ are respectively the *fast time* and *slow time* indexes, t_f is the ADC's sampling time, t_s is the sampling time in the Doppler domain, c is the speed of the light, and with

$$d_i(mt_s) = \begin{cases} d_{0,i} + x_i(mt_s) & \text{for a person} \\ d_{0,i} & \text{for clutter/objects} \end{cases}, \quad (2)$$

where d_0 indicate the absolute (or nominal) distance between the radar and the subject, and $x(mt_s)$ is vital signs information being the sub-millimeter thorax motion caused by the cardiopulmonary activity (heart and lungs). For times outside the T interval, the baseband signal is essentially zero, depending only on the noise level.

B. Data Matrix Generation

The digitized signals are arranged in two MxN matrices (Fig. 2(a)), one for each angular sector (i.e., *left matrix* and *right matrix*). Each matrix consists of N columns, containing the ADC's samples during the T_c interval of which only the samples relative to the T interval contain the target's information. Therefore, the latter is encoded in only a sub-matrix of the *left/right matrices*. More precisely, in the *left matrix*, the first columns contain the digitized baseband signals relative to TX and RX *chirps* with the antenna's beam close to 0°, while the last columns contain information about the highest scanning angle on the left. On the other hand, the *right matrix* contains information from about 0° and from the highest scanning angle on the right respectively on the first and last columns.

The following operations are described with the help of Fig. 2. In order to individuate the target's information, the two *left/right matrices* are divided in N_A sub-matrices of Mx N_c elements, where N_c is the number of samples in *fast time* we expect being influenced by a subject during T (Fig. 2(a)). In addition, we perform an overlap among the sub-matrices to have a finer angular resolution. The value of N_c and of the overlap should be set taking into account the sizes of human targets and of the typical indoor environments. For each sub-matrix, we multiply each row for a window function $w(n)$ of N_c element and we pad with zeros to have N columns. We obtain N_A sub-matrices of M xN elements which are stacked in a Mx N xN_A matrix $\mathbf{D}$ (Fig. 2(b)). More precisely, the sub-matrix $\mathbf{D}$(:,:,1) contains information from the highest scanning angular sub-sector on the left, the sub-matrix $\mathbf{D}$(:,:,2) is about the angular sub-sector right adjacent to the previous mentioned, and so on till the sub-matrix $\mathbf{D}$(:,:,N_A) which contains information from the highest scanning angular sub-sector on the right. For each row, i.e., in *fast time*, we perform the fast Fourier transform (FFT), generating the *angular/ranging matrix* $\mathbf{F}$ of Mx K xN_A elements, where each

sub-matrix $\mathbf{X}$ taken along the angular dimension, i.e., $\mathbf{F}(:,:,n_A)$ with $n_A = 1,\ldots, N_A$, is the result of the FFT-processing along a certain angular sub-sector (Fig. 2(c)). These N_A-th sub-matrix $\mathbf{X}$ can be expressed, considering only the positive frequencies and neglecting irrelevant constant phase shifts, as:

$$\begin{aligned}\mathbf{X}(m,k) &= \mathscr{F}\{ZeroPad\,[b(m,n)\cdot w(n)]\}\\ &\approx \sum_i \sum_l A_{i,l}(mt_s) W\left(\frac{k}{T_c} - \frac{B}{T_c}\frac{2d_{i,l}(mt_s)}{c}\right)\\ &\quad \cdot e^{j\left(\frac{4\pi f_c d_{i,l}(mts)}{c}\right)}\\ &\approx \sum_i \sum_l A_{i,l}(mt_s) W(k) e^{j\left(\frac{4\pi f_c d_{i,l}(mts)}{c}\right)}, \end{aligned} \tag{3}$$

with

$$W(k) = W\left(\frac{k}{T_c} - \frac{B}{T_c}\frac{2d_{i,l}(mt_s)}{c}\right), \tag{4}$$

where $\mathscr{F}$ is the FFT operator, $w(n)$ and $W(k)$ are a Fourier pair, $k = 1,...,K$ is the index of the frequency bins, with $K = N$. Since the window function in frequency domain has gradients close to zero around $2Bd_{i,l}(mt_s)/T_c$, the frequency domain window function $W(k)$ can be considered as a fixed one in *slow time*. The frequency are converted in range bins as the frequency is proportional to the range through $2B/(cT_c)$ [30]. In (3), we put B and T_c since we perform the zero-padding operation to match the *chirp* features when using non-scanning antennas. This results is an improvement of the range accuracy (limited by the radar noise) but not in range resolution (which depends only on the effective bandwidth B). Considering practical situations, we can finally limit the number of range bins to L to match the size of the monitored environment. Therefore, the number of possible path delays is also L ($l = 1,..., L$). As consequences, we obtain a significant reduction of the amount of data to be stored and processed.

Assuming P subjects and O static objects in a room, (3) can be rewritten as:

$$\mathbf{X}(m,k) = \sum_{i=1}^{P} a_i(k) e^{j\phi_i(m)} + e(k), \tag{5}$$

with

$$a_i(k) = \sum_l A_{i,l} W_{i,l}(k) e^{j\frac{4\pi f_c d_{i,l}}{c}}, \tag{6}$$

$$e(k) = \sum_{i=P+1}^{P+O} \sum_l A_{i,l} W_{i,l}(k) e^{j\frac{4\pi f_c d_{i,l}}{c}}, \tag{7}$$

$$\phi_i(m) = \frac{4\pi f_c}{c} x_i(m), \tag{8}$$

where $\phi_i(m)$ is the desired Doppler shift proportional to the thorax motion from which the vital signs rates can be measured. Each sub-matrix $\mathbf{X}$ represents a 2-D observation matrix along a certain angular sub-sector with factorization

$$\mathbf{X} = \mathbf{SH} + \mathbf{E} + \mathbf{N}, \tag{9}$$

where:

$$\mathbf{S} = \begin{bmatrix} e^{j\phi_1(1)} & \cdots & e^{j\phi_P(1)} \\ e^{j\phi_1(2)} & \cdots & e^{j\phi_P(2)} \\ \vdots & \ddots & \vdots \\ e^{j\phi_1(M)} & \cdots & e^{j\phi_P(M)} \end{bmatrix} \tag{10}$$

is a $M\times P$ complex matrix, derived from (8), containing vital signs signals from the P subjects. We assume that $\mathbf{S}$ has full rank P and each signal in each row is random, independent, and identically distributed;

$$\mathbf{H} = \begin{bmatrix} a_1(1) & \cdots & a_1(L) \\ \vdots & \ddots & \vdots \\ a_p(1) & \cdots & a_p(L) \end{bmatrix} \tag{11}$$

is an $P\times L$ complex mixing matrix derived from (6), representing the propagation channel along the n_a-th angular sub-sector;

$$\mathbf{E} = \mathbf{1}\cdot \begin{bmatrix} e(1) & \cdots & e(L) \end{bmatrix} \tag{12}$$

is an $M\times L$ matrix with identical rows containing, in *slow time*, the direct current (DC) information resulting from static reflections in the environment, where $\mathbf{1}$ is a length M all-ones column vector; and $\mathbf{N}$ is the $M\times L$ matrix containing zero mean additive noise assumed to be additive, white, complex Gaussian distributed, and independent from the sources.

C. Signal Processing

Fig. 3 shows the block diagram of the proposed signal processing technique. The angular-ranging matrix contains signals originated by: (1) the direct path reflections of the P subjects; (2) stationary and multipath reflections; (3) combination of them. The goal of the proposed data processing methodology is to identify the P independent sources, containing the vital signs information of the P subjects, and to reject the unwanted signals. As first operation, we arranged the N_A $\mathbf{X}$ sub-matrices (Fig. 2(c)) into a 2-D combined matrix $\mathbf{Y}$ (Fig. 3). Mathematically, it can be expressed as:

$$\mathbf{Y} = \mathbf{SG} + \mathbf{E_G} + \mathbf{N_G}, \tag{13}$$

where:

$$\mathbf{G} = \begin{bmatrix} a_1(1) & \cdots & a_1(N_A L) \\ \vdots & \ddots & \vdots \\ a_p(1) & \cdots & a_p(N_A L) \end{bmatrix} \tag{14}$$

is the $P\times(N_A\cdot L)$ overall propagation channel matrix, with $\mathbf{E_G}$ and $\mathbf{N_G}$ being $P\times(N_A\cdot L)$ containing the contributions of the static reflectors and noise, respectively.

We then remove the DC contributions of static reflectors (e.g., objects, furniture, walls, static parts of the human body, etc.). We achieve this by removing $\mathbf{E_G}$ in $\mathbf{Y}$ using a projection matrix $\mathbf{J}$ such that $\mathbf{JE_G} = \mathbf{0}$. The result of this operation is:

$$\mathbf{JY} = \mathbf{JSG} + \mathbf{JE_G} + \mathbf{JN_G} = \mathbf{JGS} + \mathbf{JN_G}. \tag{15}$$

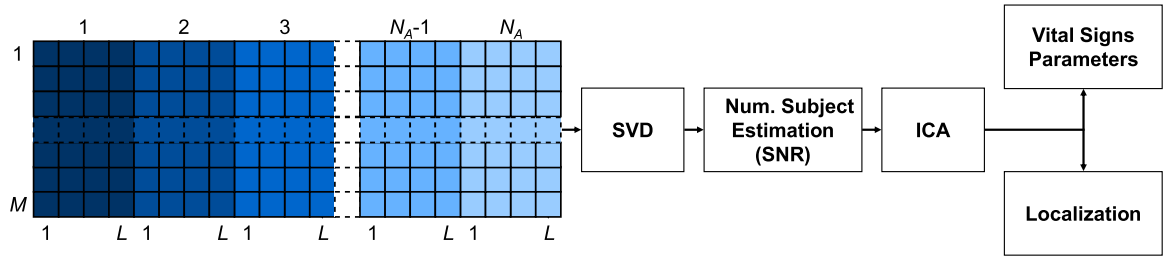

Fig. 3. Block diagram of the signal processing technique. The angular-ranging matrix of Fig. 2(c) is combined into a 2-D matrix.

Considering

$$\overline{\mathbf{Y}} = \mathbf{JY}, \tag{16}$$

$$\overline{\mathbf{S}} = \mathbf{JS}, \tag{17}$$

$$\overline{\mathbf{N_G}} = \mathbf{JN_G}, \tag{18}$$

(15) becomes

$$\overline{\mathbf{Y}} = \overline{\mathbf{S}}\mathbf{G} + \overline{\mathbf{N_G}}. \tag{19}$$

The next objective is to determine the P sources. To achieve this goal, we first perform the economy-sized singular value decomposition (SVD) over the $N_A{\cdot}L$ columns of $\overline{\mathbf{Y}}$ in *slow time*. Therefore, $\overline{\mathbf{Y}}$ can be factorized as:

$$\overline{\mathbf{Y}} = \overline{\mathbf{S}}\mathbf{G} + \overline{\mathbf{N_G}} = \mathbf{U} \cdot \mathbf{\Sigma} \cdot \mathbf{V^H}, \tag{20}$$

where $\mathbf{U}$ is an $M \times N_A{\cdot}L$ matrix containing left singular vectors, $\mathbf{\Sigma}$ is an $N_A{\cdot}L \times N_A{\cdot}L$ diagonal matrix containing all the singular values, and $\mathbf{V}$ is an $N_A{\cdot}L \times N_A{\cdot}L$ matrix containing right singular vectors and its $\mathbf{H}$ superscript indicates the Hermitian transpose. $\mathbf{U}$ is a complex matrix whose first P columns contain the uncorrelated sources of the P subjects whereas the remaining columns can be treated as noise. In order to determine P, we propose an approach based on the estimation of the signal-to-noise ratio (SNR) of the signals of $\mathbf{U}$. We exploit the fact that the spectrum of a typical radar-based vital signs signal consists mainly of the dominant respiration's fundamental and few decreasing in magnitude respiration harmonics. The heartbeat's fundamental is very small and its contribution can be neglected in the signal. Therefore, we define as *signal power* the power due to the respiration fundamental and its first two harmonics, while the rest of the spectrum is considered as *noise*. We perform linear demodulation on $\mathbf{U}$ in *slow time*. This operation (details in [59]) provides the phase information, namely the Doppler signals, relative to the complex uncorrelated signals. The SNR is estimated for each Doppler signal. First, we calculate the *signal power*'s value integrating the parts of the spectrum corresponding to the respiration's peak f_r, which is the highest value, and to its two first harmonics, which are at $2f_r$ and $3f_r$. Since each Doppler signal is low pass filtered at 6 Hz, the *noise power* is calculated integrating the spectrum in the (0, 6] Hz interval and subtracting to it the *signal power*'s value. We then calculate their SNRs. The first P uncorrelated sources producing an SNR over a threshold are considered to be relative to the P subjects. The other sources are treated as noise, hence discarded. The next step is to apply the independent component analysis (ICA) to the P uncorrelated sources. This allows estimating the statistically independent sources $\hat{\mathbf{S}}$. We can finally perform on them the linear demodulation. The results are the Doppler signals of the P subjects as in (8), from which we can extract the vital signs parameters after proper filtering and frequency analysis (examples are shown and discussed in Section IV).

At this stage, we have determined the P sources $\hat{\mathbf{S}}$ (hence, the vital signs signals). We have now to determine from which locations of the environment they are sensed. This means that we have to determine the l-th range bin and the n_a-th angular sub-sector relative to each source. In doing so, we arrange $\overline{\mathbf{Y}}$ in an Mx L xN_A matrix and we perform the following procedure per each of its N_A $\overline{\mathbf{X}}$ sub-matrices. First, we tackle the effect of the path loss in each sub-matrix. Due to that, the columns (i.e., observation vectors) in $\overline{\mathbf{H}}$ have unequal power. Therefore, in order to balance the residual errors, we perform a column-wise normalization on $\overline{\mathbf{X}}$. Defining $\overline{\overline{\mathbf{X}}}$ as the normalized version of $\overline{\mathbf{X}}$ and $\mathbf{A}$ as the diagonal scaling matrix, we obtain:

$$\overline{\overline{\mathbf{X}}} = \overline{\mathbf{X}}\mathbf{A} = \hat{\mathbf{S}}\mathbf{H}\mathbf{A} = \hat{\mathbf{S}}\overline{\mathbf{H}}. \tag{21}$$

We then estimate the energy of the sources by minimizing the residual error, as:

$$\min_{\overline{\mathbf{H}}} \|\overline{\overline{\mathbf{X}}} - \hat{\mathbf{S}}\overline{\mathbf{H}}\|_2^2 + \zeta\|\overline{\mathbf{H}}\|_1, \tag{22}$$

where ζ is the penalty coefficient, representing a trade-off between the residual error and the sparsity. Since the scaling matrix $\mathbf{A}$ is known, we estimate the channel response of the sources P as

$$\hat{\mathbf{H}} = \overline{\mathbf{H}}\mathbf{A}. \tag{23}$$

The result of this operation is a $P{\times}L$ matrix. Each i-th row is the channel response of the i-th subject along the n_a-th orientation. We repeat the aforementioned procedure N_A times. Thus, we obtain P $N_A{\times}L$ matrices, each containing the 2-D channel response of each subject. The target's position is determined searching in its relative matrix, the most significant value. The corresponding indices (n_a, l) indicates the subject's 2-D position (examples are in Section IV).

III. Radar System

Fig. 4 shows a photo of the radar sensor. Its core is the imec's 8 GHz FMCW radar chip which integrates the *chirp*

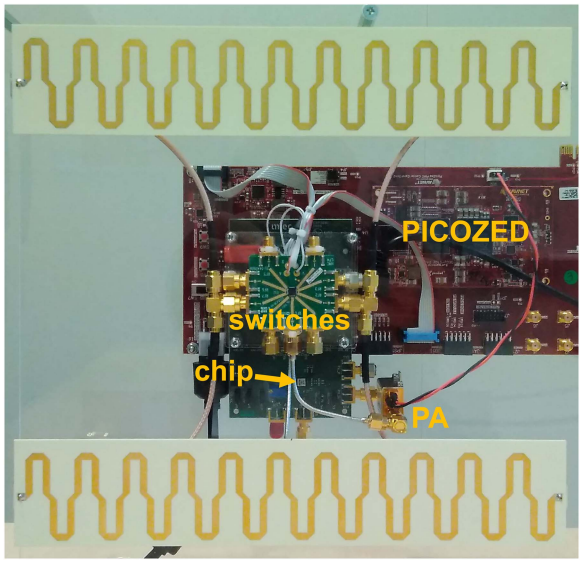

Fig. 4. Radar sensor.

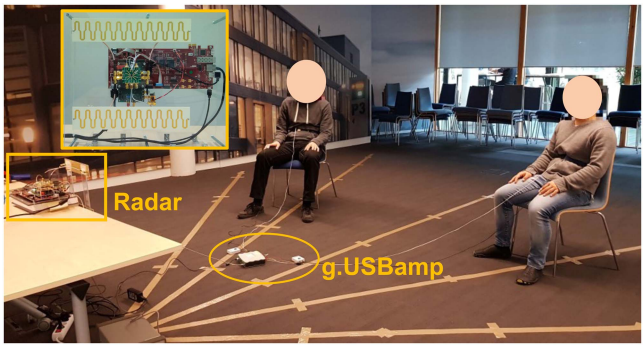

Fig. 5. Experimental set-up.

source, an LNA, a mixer, whose output is band pass filtered, and a 9-bit ADC. Details on the chip design and architecture are reported in [24], [25]. As external devices, we used the EV1HMC321ALP4E 8-switch board and the Mini-Circuits ZX60-06203LN+ power amplifier (PA). A Picozed board acquires and sends the ADC samples to Matlab.

Each *chirp* has a duration of $T = 40.96$ μs and a total bandwidth B of 1 GHz, from $f_0 = 7.3$ GHz to $f_1 = 8.3$ GHz. This involves a range resolution of 15 cm. Therefore, the subjects are expected to be located in range at multiples of 15 cm (i.e., 0 cm, 15 cm, 30 cm, 45 cm,...). The ADC's sample frequency f_{ADC} is of 12.5 MHz. This results in 512 samples acquired in *fast time* during T. The *chirps* are transmitted with a pulse repetition interval (PRI) of 1.3 ms. Since two *chirps* are required to scan the whole environment, the effective sampling time in *slow time* t_s is of 2.6 ms.

The radar is connected to two identical FSAs (one as TX and the other as RX), designed to operate in the same bandwidth of the *chirp* (Fig. 4(a)). Details on the antenna design and testing have been reported by the Authors in [66]. Those antennas allow a maximum angular scan of 60° as per direction of rotation (i.e., clockwise and counterclockwise), with a gain varying inside the 12.4 dB–15.8 dB range and with a 3 dB beamwidth which varies from 8.5° at 7.3 GHz to 17.7° at 8.3 GHz. A power of about −10 dBm is applied to the TX antenna.

A. Link Budget Analysis

From the radar theory [68], the power of the received signal P_{re} can be expressed as:

$$P_{re} = \frac{P_{tr} G_t G_r \lambda_1^2 \sigma}{(4\pi)^3 D^4 L_s}. \tag{24}$$

where P_{tr} is the power of the transmitted signal, G_t and G_r are respectively the transmitting and receiving antennas' gains, λ_1 is wavelength corresponding to f_1 (we considered the worst case), σ is the radar cross section (RCS), D is the target's absolute distance, and L_s takes into the account the receiver losses (e.g., cables, microstrips, etc.). In this analysis, we considered $\sigma = -16$ dBsm as the RCS of the chest of a person, and $D = 4$ m as maximum range. In addition, the imec's chip has the following parameters: $P_{tr} = -10$ dBm, $G_t = G_r = 14$ dBi (we considered the average value), $\lambda_1 = 0.0361$ m, noise figure $F = 12.5$ dB, $L_s = 3$ dB, $N = 512$ baseband samples per chirp ($T = 40.96$ μs), and a receiver bandwidth $B_w = f_{ADC}/2 = 6.25$ MHz [24]. Since the radar system integrates a switch board of 2.5 dB loss as first block of the receiver, we can consider a total noise figure F of 15 dB. With these parameters, the thermal noise power $P_n = kT_0FB_w$ is −91 dBm, where $kT_0 = -174$ dBm is the product between the Boltzmann's constant and the standard ambient temperature [68]. From (24), a subject at 4 m would produce a reflected signal with a P_{re} of about −87 dBm. In reality, the signal of interest occupies a bandwidth smaller than the maximum Nyquist bandwidth B_w. In fact, the estimation of the number of subjects is performed after 1-stage FFT followed by a low-pass filter in *slow time*. More precisely, the baseband signal is first multiplied by a Hanning window and then FFT is performed. This involved a process gain PG_1 of $10\log(B_w/f_{ADC}/N{*}window\_gain) = 21$ dB, with $window\_gain = 0.5$. The slow time signal, sampled with a frequency rate of about 385 Hz ($t_s = 2.6$ ms), is then low-pass filtered at 6 Hz. This involves another process gain PG_2 of 18 dB. The total process gain is $PG = PG_1 + PG_2 = 39$ dB. For a subject at 4 m, the system presents a theoretical SNR = P_{re}(4 m) - $P_n + PG = -87 + 91 + 39 = 43$ dB.

B. Phase Noise Analysis

The SNR formulation of Section III.A compares the power levels of the received signal and of the thermal noise. However, for a radar based vital signs monitoring system, the main challenge is to detect the very small phase (Doppler) shift caused by the heart activity. Therefore, we should consider also the phase SNR defined as the ratio between the heartbeat phase excursion and the phase noise. The root-mean square (RMS) phase noise $\Delta\Phi_{RMS}$ on a carrier frequency is directly proportional to the thermal noise at the input and the noise figure of the receiver [68].

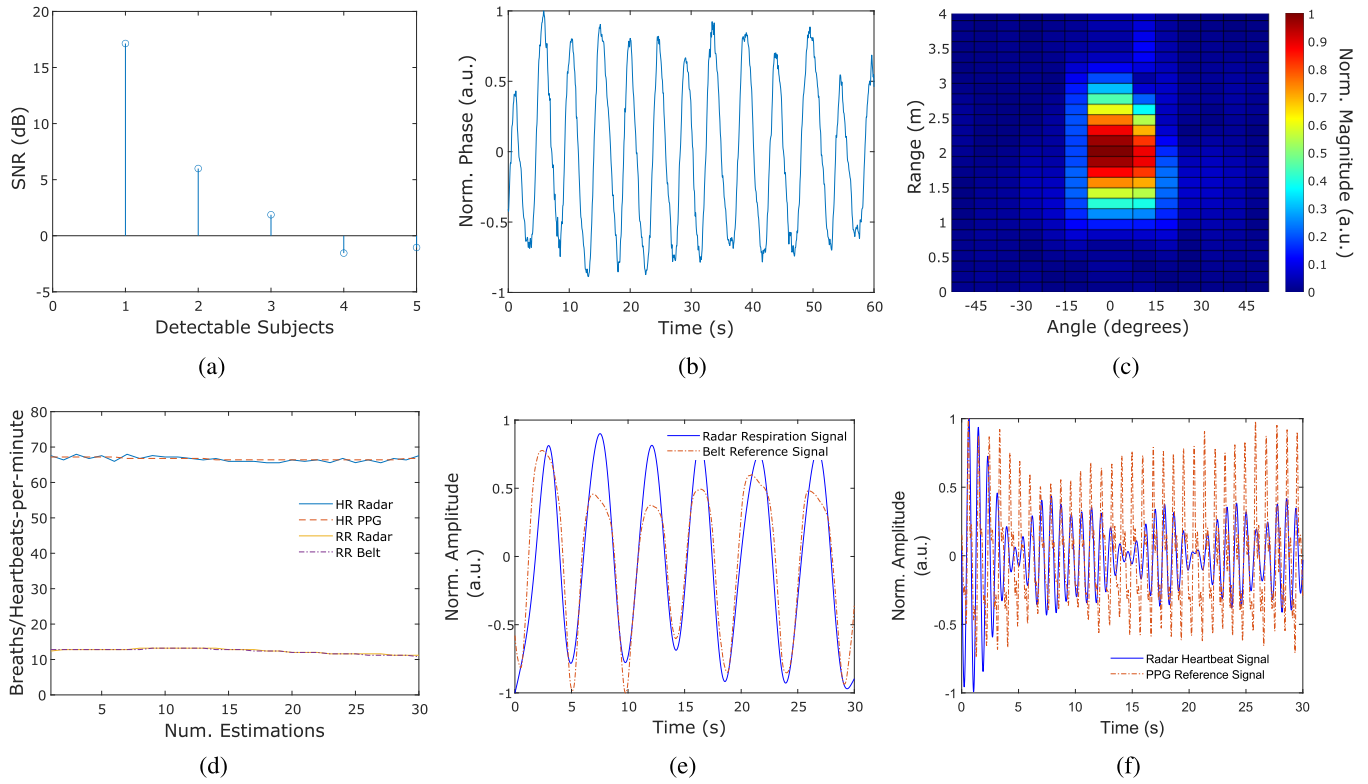

Fig. 6. Experimental results with a subject at 2 m and 0°. (a) Estimation of the number of subjects present in the room. (b) Retrieved source. (c) 2-D channel response. (d) Vital signs rates and comparison with the references.(e) Time domain comparison between the extracted radar respiratory signal and the belt signal. (f) Time domain comparison between the extracted radar heartbeat signal and the PPG signal.

It can be expressed as:

$$\Delta\Phi_{RMS} = \sqrt{\frac{kT_0FB_w}{P_{re}}}. \tag{25}$$

The vital signs rates are extracted after two stages of FFT. The first stage is applied in *fast time* involving a power gain PG_1 of 21 dB. The second stage is applied in *slow time* on the phase information (Doppler signal) of the estimated sources $\hat{\mathbf{S}}$. Since the FFT is applied on Doppler signals of 30 seconds sampled in *slow time* at about 385 Hz ($t_s = 2.6$ ms), this involves another power gain PG_3 of 38 dB, i.e., 10log(385*30*$window\_gain$). The total signal processing power gain is $PG = PG_1 + PG_3 = 59$ dB. Therefore, the accurate formula to compute the RMS phase noise $\Delta\Phi_{RMS}$ becomes:

$$\Delta\Phi_{RMS} = \sqrt{\frac{kT_0FB_w}{P_{re}} \cdot \frac{1}{PG}}. \tag{26}$$

Assuming 0.1 mm as the amplitude of the heart motion x on the thorax surface, the corresponding RMS Doppler shift is about $4\pi x/\lambda_0 = 0.0306$ rd. Positioning a subject at 2 m, 3 m, and 4 m, the estimated RMS phase noises are 0.00017 rd, 0.00037 rd, and 0.00066 rd, respectively. Therefore, the resulting phase SNRs are respectively 45.28 dB, 38.24 dB, and 33.24 dB. Although in practice the SNR values are lower than the theoretical ones, this analysis gives enough confidence that the proposed radar system is capable to properly monitor the vital signs of a subjects within 4 m.

In determining the number of targets, we consider from the Doppler signals the respiratory signals, whose energies are essentially contained into the fundamentals. Assuming as worst case 1 mm as the amplitude of lungs' motion on the thorax surface, the corresponding RMS Doppler shift is about 0.306 rd. Considering that each estimated Doppler signal is low-pass filtered at 6 Hz, and following the above formulation, the corresponding estimated RMS phase noises for a subject at 2 m, 3 m, and 4 m, are respectively 0.0024 rd, 0.0053 rd, and 0.0094 rd, which theoretical phase SNRs are of 42.11 dB, 35.23 dB, and 30.25 dB, respectively. However, in practice, we normally subtract 20 dB to the theoretical values. This justifies why, in this work, we considered a threshold of 10 dB in estimating P subjects.

IV. Experimental Results

We conducted the experimental evaluations in a lab environment (Fig. 5). All procedures in this study adhered to the ethical principles of the Declaration of Helsinki. Written informed consent was provided by all patients before they were enrolled in the study. The IMEC ethical board reviewed and approved the study protocols (IP-19-WATS-TIP2-056). All the collected data were pseudonymized. The radar sensor was put at about 1 m of height on a desk. We used as gold standard reference the g.USBamp medical device. It integrates photoplethysmogram

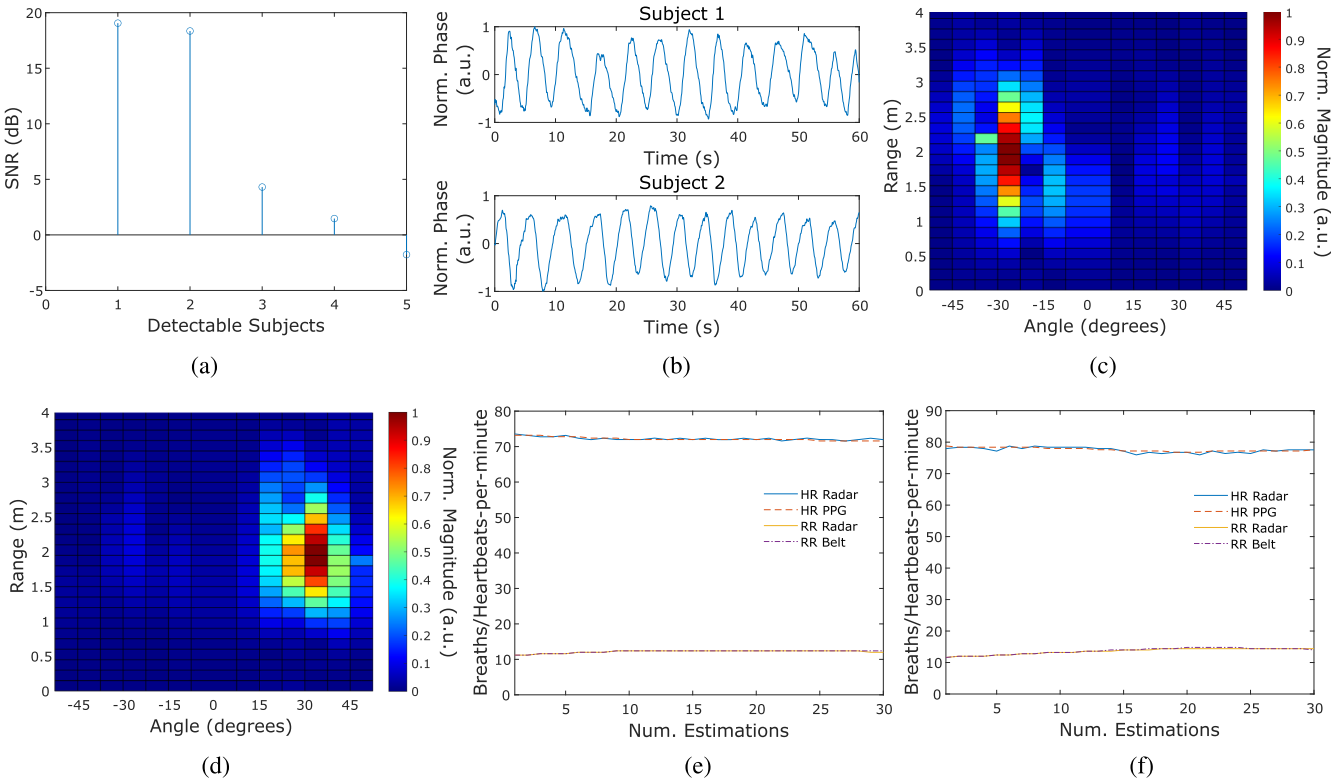

Fig. 7. Experimental results with two subjects at 2 m and $\pm 30^{\circ}$. (a) Estimation of the number of subjects present in the room. (b) Retrieved sources. (c) 2-D channel response of Subject 1. (d) 2-D channel response of Subject 2. (e) Vital signs rates of Subject 1 and comparison with the references. (f) Vital signs rates of Subject 2 and comparison with the references.

(PPG) finger sensors and respiration belts to measure the heartbeat and respiration, respectively. We marked traces on the floor to have information on the absolute distances and the angular orientations of the volunteers.

The *left/right matrices* consist of $N = 512$ samples in *fast time*. In this work, we have chosen $N_c = 64$ with 50% overlap. This results in $N_A = 14$. Thus, considering that the radar can scan a total angular range of $\pm 60^{\circ}$, we divide the monitored environment in 14 equal-spaced angular sectors, namely from 0° to $\pm 15^{\circ}$, from $\pm 7.5^{\circ}$ to $\pm 22.5^{\circ}$, from $\pm 15^{\circ}$ to $\pm 30^{\circ}$, from $\pm 22.5^{\circ}$ to $\pm 37.5^{\circ}$, from $\pm 30^{\circ}$ to $\pm 45^{\circ}$, from $\pm 37.5^{\circ}$ to $\pm 52.5^{\circ}$, and from $\pm 45^{\circ}$ to $\pm 60^{\circ}$. This means that a subject would be oriented in the middle of an angular sub-sector, namely at $\pm 7.5^{\circ}$, $\pm 15^{\circ}$, $\pm 22.5^{\circ}$, $\pm 30^{\circ}$, $\pm 37.5^{\circ}$, $\pm 45^{\circ}$, and $\pm 52.5^{\circ}$. This involves a maximum angular error of 3.5°. A different consideration is required for a target at 0°. In this case, it will be located at $\pm 7.5^{\circ}$, involving a maximum angular error of 7.5°. For each m, the N_c samples are multiplied by a Hanning window, zero padded to N, and then the FFT is performed. The result of this operation is an $M \times 512 \times 14$ angular-ranging matrix (Fig. 3(c)). Since each measure is of 1 minute, we have $M = 23077$ samples in *slow time* ($t_s = 2.6$ ms). As the room is limited in size, we consider only the first $L = 30$ range bins (i.e., up to 4.5 m). Therefore, the signal processing is performed on an angular-ranging matrix of $23077 \times 30 \times 14$ elements.

Fig. 6 shows the results of an experiment with a normally breathing subject seated at 2 m and 0° . The algorithm detects one subject present in the room. In fact, as shown in Fig. 6(a), there is only one value above 10dB in the SNR plot of the uncorrelated sources. The extracted Doppler signal is shown in Fig. 6(b). It was obtained by low-pass filter at 6 Hz the estimated Doppler signal. Its channel response is reported in 6(c). Due to the subject's size, to the zero padding and FFT operations, there are some significant values in the channel response. However, the peak, corresponding to the subject position, is at 1.95 m (i.e., the multiple of the range resolution closest to 2 m) and -7.5° . In Fig. 6(d), we show the vital signs rates over time compared to the references. The respiration and heartbeat signals are extracted using band-pass filters with frequency bands respectively of 0.1–0.4 Hz and of 1–1.5 Hz. The corresponding rates are determined by FFT. We reported maximum errors of 1.2 heartbeats-per-minute (HPM) and 0.4 breaths-per-minute (BPM) respectively for the heart rate (HR) and respiration rate (RR). In determining, the vital signs rates, we considered a sliding window approach with a signal length of 30s and shifts of 1s for a total of 30 estimations. We also zero padded each window signal of a factor 5 times its original size. This corresponds to a resolution of 0.4 BPM/HPM. These small differences, which can be considered clinically acceptable [69], [70], [71], are mainly due to the fact that the reference signals are acquired with wearable devices which are less sensitive to noise and interference than contactless devices as the radar. In Fig. 6(e), (f), we report the time domain comparisons between the respiratory and heartbeat signals with their corresponding references. The

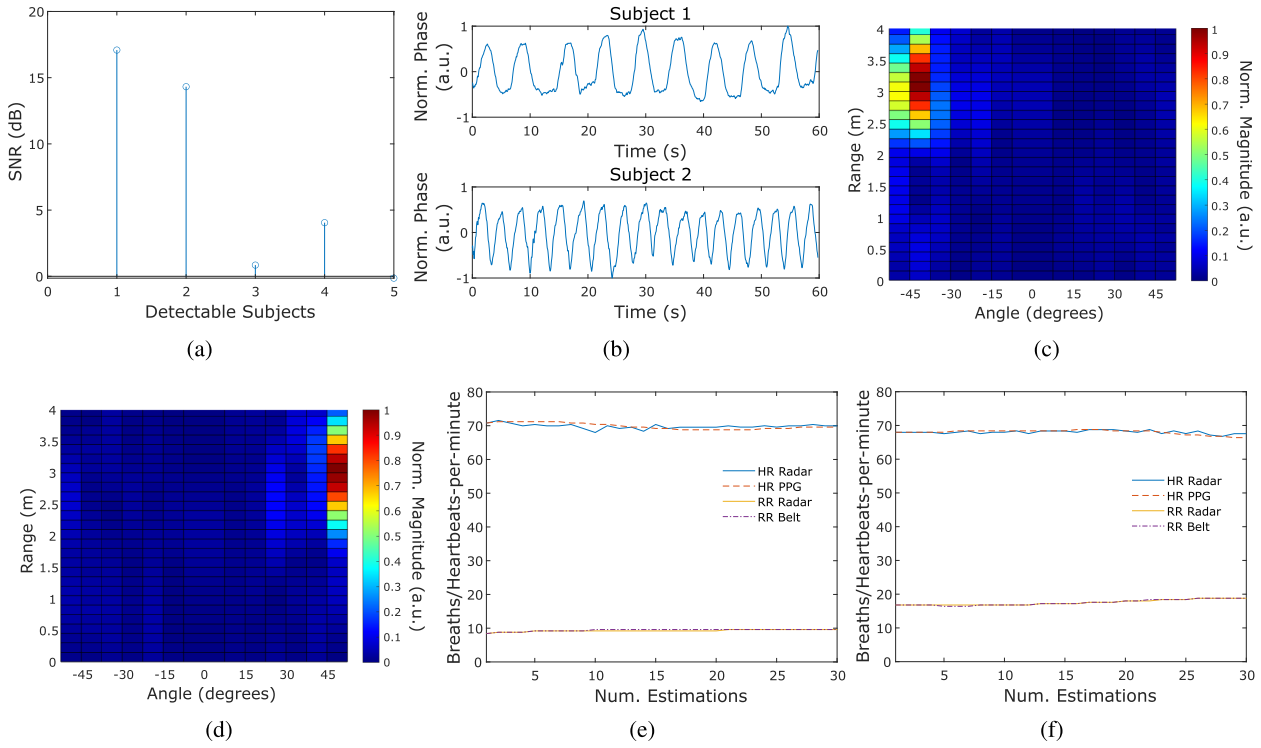

Fig. 8. Experimental results with two subjects at 3 m and $\pm 45°$. (a) Estimation of the number of subjects present in the room. (b) Retrieved sources. (c) 2-D channel response of Subject 1. (d) 2-D channel response of Subject 2. (e) Vital signs rates of Subject 1 and comparison with the references. (f) Vital signs rates of Subject 2 and comparison with the references.

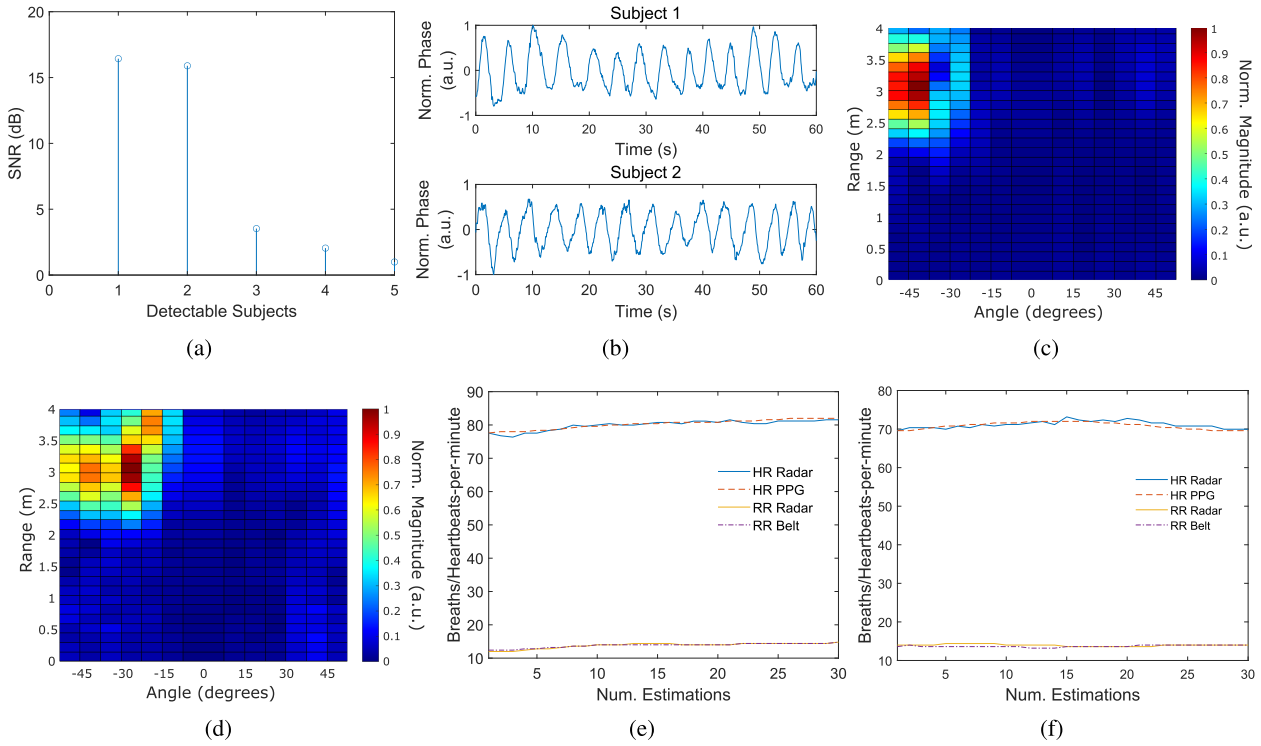

Fig. 9. Experimental results with two subjects. Subject 1 seated at 3 m and $-45°$ while Subject 2 at 3 m and $-30°$. (a) Estimation of the number of subjects present in the room. (b) Retrieved sources. (c) 2-D channel response of Subject 1. (d) 2-D channel response of Subject 2. (e) Vital signs rates of Subject 1 and comparison with the references. (f) Vital signs rates of Subject 2 and comparison with the references.

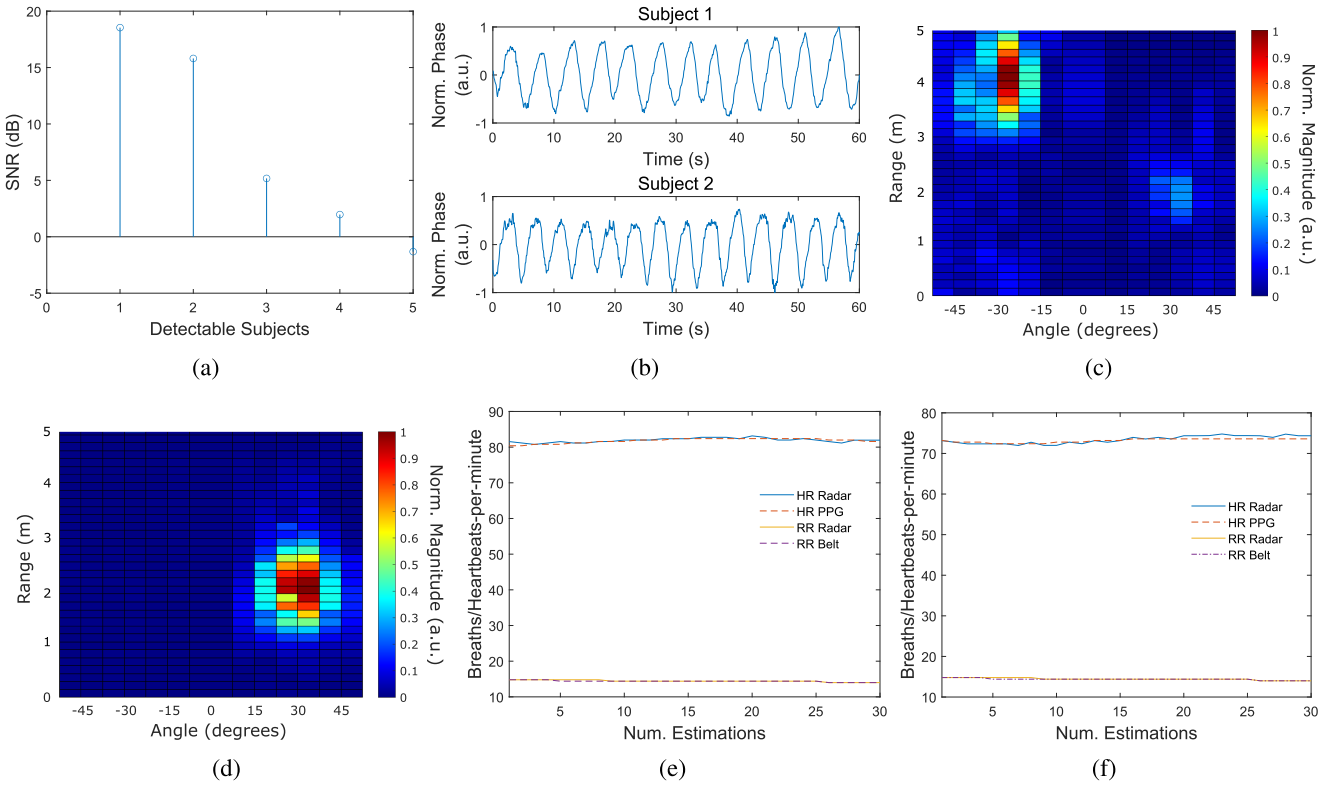

Fig. 10. Experimental results with two subjects. Subject 1 seated at 4 m and -30° and Subject 2 at 2 m and 30°. (a) Estimation of the number of subjects present in the room. (b) Retrieved sources. (c) 2-D channel response of Subject 1. (d) 2-D channel response of Subject 2. (e) Vital signs rates of Subject 1 and comparison with the references. (f) Vital signs rates of Subject 2 and comparison with the references.

TABLE I
COMPARISON WITH ALTERNATIVE STATE-OF-THE-ART SOLUTIONS

Ref. no.	Radar type	Needs info no. subject	Max dist. (m)	Range info	Range max error (cm)	Azimuth info	Angle max error (°)	BPM MAE	HPM MAE
[9]	SIMO CW	YES	3	NO	N.A.	YES	5	N.A.	N.A.
[40]	MIMO CW	YES	1.8	NO	N.A.	YES	2	< 1	< 1
[41]	MIMO FMCW	NO	3	YES	40	YES	8	< 2	Not able
[42]	Phased-MIMO FMCW	YES	4	YES	N.A.	YES	N.A.	0.66	3.02
[48]	Distributed MIMO CW	YES	1.9	YES	7	YES	2.52	0.6	2.4
[52]	MIMO FMCW	YES	2	YES	N.A.	YES	N.A.	< 1	< 5
[54]	Scanning FMCW	YES	4.3	YES	6.6	YES	N.A.	N.A.	N.A.
This work	FSA FMCW	NO	4	YES	7.5	YES	3.5*	0.09	0.47

*The angle max error is 7.5° only when the beam points to 0°.

extracted respiratory signal fairly follows the corresponding belt signal. This is also true in the case of the heartbeat signal although, in this case, there can be seen tiny misalignments, due to the same reasons which cause the differences in the rates' estimations.

Fig. 7 shows the results of an experiment with two normally breathing subjects seated at 2 m and $\pm 30^\circ$. The algorithm detects properly the number of subjects (Fig. 7(a)) whose vital signs signals are reported in Fig. 7(b). The volunteers have been located at 1.95 m and $\pm 30^\circ$ (Fig. 7(c), (d)). For Subject 1, we reported maximum errors of 0.8 HPM and 0.4 BPM respectively for the HR and RR (Fig. 7(e)). For Subject 2, we reported maximum errors of 1.2 HPM and 0.4 BPM respectively for the HR and RR (Fig. 7(f)).

Fig. 8 shows the results of an experiment with two subjects at 3 m and $\pm 45^\circ$. Also in this case, we report satisfactory results. The targets have been located at 3 m and $\pm 45^\circ$ (Fig. 8(c), (d)). For Subject 1, we reported maximum errors of 2.4 HPM and 0.4 BPM (Fig. 8(e)) while, for Subject 2, they are respectively of 1.2 HPM and 0.4 BPM (Fig. 8(f)).

In Fig. 9, we reported the results of an experiment with two subjects, seated at the same range bin and separated by one angular resolution. Subject 1 is at 3 m and $-45°$ and Subject 2 is at 3 m and $-30°$. This situation can be found in several everyday life situations, such as people seated around a table or on a couch, students seated in school desks, etc. The algorithm detects accurately the two subjects (Fig. 9(a)). Subject 1 is located at 3 m and $-45°$, reporting maximum errors of 1.6 HPM and 0.4 BPM (Fig. 9(e)). Subject 2 is located at 3 m and $-30°$, with errors of 1.6 HPM and 0.8 BPM (Fig. 9(f)).

In Fig. 10, we reported the results of an experiment with two subjects at different distances. Subject 1 is seated at 4 m and $-30°$ while Subject 2 at 2 m and 30°. Subject 1 is located at 4.05 m and $-30°$ while Subject 2 at 1.95 m and 30° (Fig. 10(c), (d)). In both cases, there is an error of 5 cm in determining the range information. This is expected since the targets have been properly located at the closest integer multiple of the range resolution. Regarding the vital signs, for both subjects, we report errors of 1.2 HPM and 0.4 BPM (Fig. 10(e), (f).

Finally, in Table I, we compare the proposed work with alternative state-of-the-art approaches. The results show that this work, although proposing a simpler architecture, achieves comparable or even better performance both in 2-D localization and in vital signs monitoring. Regarding the vital signs rates, the mean absolute error (MAE) is the metric used to determine the HR and the RR accuracy in accordance with the ANSI/AAMI EC13:2002 standard. MAEs less than or equal to 5 HPM and to 3 BPM are considered clinically acceptable [69], [70], [71].

V. Conclusion

In this work, we proposed and discussed a signal processing technique for concurrent localization and life-sign detection of people in indoor environment. The algorithm is able to distinguish the individual Doppler contribution of each subject, enabling remote people monitoring. We demonstrated experimentally the feasibility of the proposed approach using an FMCW radar which integrates two FSAs. Anyhow, the approach is valid for any beam-scanning radar architecture. Practical applications arise for healthcare, Hospital 4.0, patient/neonatal monitoring in intensive care units, geriatric and quarantine medicine, ambient assisted living, automotive, rescue and security purposes. Future goal is to extend the proposed algorithm for: (1) monitoring moving subjects (e.g., walking around, fall detection); (2) identify pets; (3) distinguishing moving clutter (e.g., a ventilator); (4) monitoring the vital signs of seated/lying down subjects in presence of moving subjects (e.g., caregivers).

References

[1] J.-C. Chiao et al., "Applications of microwaves in medicine," *IEEE J. Microw.*, vol. 3, no. 1, pp. 134–169, Jan. 2023.

[2] C. Li, "Vital-sign monitoring on the go," *Nature Electron.*, vol. 2, pp. 219–220, Jun. 2019.

[3] D. Schreurs and M. Mercuri, "Contactless medical sensing," in *Proc. IEEE MTT-S Int. Microw. Symp. Dig.*, May 2015, pp. 1–4.

[4] C. Li et al., "Sensing of life activities at the human-microwave frontier," in *Proc. IEEE J. Microw.*, vol. 1, no. 1, pp. 66–78, Jan. 2021.

[5] J. C. Lin, "The microwave auditory effect," *IEEE J. Electromagn., RF, Microw. Med. Biol.*, vol. 6, no. 1, pp. 16–28, Mar. 2022.

[6] C. Li et al., "A review on recent advances in doppler radar sensors for noncontact healthcare monitoring," *IEEE Trans. Microw. Theory Techn.*, vol. 61, no. 5, pp. 2046–2060, May 2013.

[7] F.-K. Wang, J.-X. Zhong, and J.-Y. Shih, "IQ signal demodulation for noncontact vital sign monitoring using a CW Doppler radar: A review," *IEEE J. Electromagn., RF, Microw. Med. Biol.*, vol. 6, no. 4, pp. 449–460, Dec. 2022.

[8] A. D. Droitcour et al., "Range correlation and I/Q performance benefits in single-chip silicon Doppler radars for noncontact cardiopulmonary monitoring," *IEEE Trans. Microw. Theory Techn.*, vol. 52, no. 3, pp. 838–848, Mar. 2004.

[9] H. Zhao et al., "A noncontact breathing disorder recognition system using 2.4-GHz Digital-IF doppler radar," *IEEE J. Biomed. Health Inform.*, vol. 23, no. 1, pp. 208–217, Jan. 2019.

[10] C. Gu et al., "Accurate respiration measurement using DC-coupled continuous-wave radar sensor for motion-adaptive cancer radiotherapy," *IEEE Trans. Biomed. Eng.*, vol. 59, no. 11, pp. 3117–3123, Nov. 2012.

[11] D. Buxi et al., "Systolic time interval estimation using continuous wave radar with on-body antennas," *IEEE J. Biomed. Health Inform.*, vol. 22, no. 1, pp. 129–1391, Jun. 2018.

[12] C. Garripoli et al., "Embedded DSP-Based telehealth radar system for remote in-door fall detection," *IEEE J. Biomed. Health Inform.*, vol. 19, no. 1, pp. 92–101, Jan. 2015.

[13] I. Mostafanezhad et al., "A low cost simple RF front end using time-domain multiplexing for direction of arrival estimation of physiological signals," in *Proc. IEEE MTT-S Int. Microw. Symp. Dig.*, Jun. 2013, pp. 1–4.

[14] F. K. Wang et al., "A novel vital-sign sensor based on a self-injection-locked oscillator," *IEEE Trans. Microw. Theory Techn.*, vol. 58, no. 12, pp. 4112–4120, Dec. 2010.

[15] F. K. Wang et al., "Single-antenna doppler radars using self and mutual injection locking for vital sign detection with random body movement cancellation," *IEEE Trans. Microw. Theory Techn.*, vol. 59, no. 12, pp. 3577–3587, Dec. 2011.

[16] M.-C. Tang, F.-K. Wang, and T.-S. Horng, "Single self-injection-locked radar with two antennas for monitoring vital signs with large body movement cancellation," *IEEE Trans. Microw. Theory Techn.*, vol. 65, no. 12, pp. 5324–5333, Dec. 2017.

[17] M. Mercuri et al., "Frequency-tracking CW doppler radar solving small-angle approximation and null point issues in non-contact vital signs monitoring," *IEEE Trans. Biomed. Circuits Syst.*, vol. 11, no. 3, pp. 671–680, Jun. 2017.

[18] M. Mercuri et al., "A direct phase-tracking doppler radar using wavelet independent component analysis for non-contact respiratory and heart rate monitorin," *IEEE Trans. Biomed. Circuits Syst.*, vol. 12, no. 3, pp. 632–643, Jun. 2018.

[19] E. Schires, P. Georgiou, and T. S. Lande, "Vital sign monitoring through the back using an UWB impulse radar with body coupled antennas," *IEEE Trans. Biomed. Circuits Syst.*, vol. 12, no. 2, pp. 292–302, Apr. 2018.

[20] X. Liang et al., "Ultra-wideband impulse radar through-wall detection of vital signs," *Sci. Rep.*, vol. 8, no. 13367, pp. 1–21, Sep. 2018.

[21] M. Mercuri et al., "Optimised waveform design for radar sensor aimed at contactless health monitoring," *Electron. Lett.*, vol. 48, no. 20, pp. 1255–1257, Sep. 2018.

[22] J. Wang et al., "A spectrum-efficient FSK radar technology for range tracking of both moving and stationary human subjects," *IEEE Trans. Microw. Theory Techn.*, vol. 67, no. 12, pp. 5406–5416, Dec. 2019.

[23] M. Mercuri et al., "Digital linear discrete FMCW radar for healthcare applications," in *Proc. IEEE MTT-S Int. Microw. Symp. Dig.*, Jun. 2019, pp. 144–147.

[24] Y.-H. Liu et al., "9.3 A680 μW burst-chirp UWB radar transceiver for vital signs and occupancy sensing up to 15 m distance," in *Proc. IEEE ISSCC Dig. Tech. Papers*, Feb. 2019, pp. 166–167.

[25] Y.-H. Liu et al., "An ultralow power burst-chirp UWB radar transceiver for indoor vital signs and occupancy sensing in 40-nm CMOS," *IEEE Solid-State Circuits Lett.*, vol. 2, no. 11, pp. 256–259, Nov. 2019.

[26] A. A. Pramudita et al., "Radar system for detecting respiration vital sign of live victim behind the wall," *IEEE Sensors J.*, vol. 22, no. 15, pp. 14670–14685, Aug. 2022.

[27] M. Mercuri et al., "Biomedical radar system for real-time contactless fall detection and indoor localization," *IEEE J. Electromagn., RF, Microw. Med. Biol.*, vol. 7, no. 4, pp. 303–312, Dec. 2023.

[28] Q. Wu et al., "A non-contact vital signs detection in a multi-channel 77 GHz LFMCW radar system," *IEEE Access*, vol. 9, pp. 49614–49628, 2021.

[29] F. Adib et al., "Multi-person localization via RF body reflections," in *Proc. 12th USENIX Symp. Networked Syst. Des. Implementation*, May 2015, pp. 279–292.
[30] M. Mercuri et al., "Vital-sign monitoring and spatial tracking of multiple people using a contactless radar-based sensor," *Nat. Electron.*, vol. 2, pp. 252–262, Jun. 2019.
[31] A. Bin-Obadi et al., "A survey on vital signs detection using radar techniques and processing with FPGA implementation," *IEEE Circuits Syst. Mag.*, vol. 21, no. 1, pp. 41–74, Firstquarter 2021.
[32] W. Su et al., "Stepped-frequency continuous-wave radar with self-injection-locking technology for monitoring multiple human vital signs," *IEEE Trans. Microw. Theory Techn.*, vol. 67, no. 12, pp. 5396–5405, Dec. 2019.
[33] G. Sacco et al., "A radar system for indoor human localization and breath monitoring," in *2018 IEEE Int. Symp. Med. Meas. Appl.*, Jun. 2018, pp. 1–6.
[34] G. Sacco et al., "An FMCW radar for localization and vital signs measurement for different chest orientations," *Sensors*, vol. 20, no. 12, pp. 1–14, Jun. 2020.
[35] G. Wang et al., "Application of linear-frequency-modulated continuous-wave (LFMCW) radars for tracking of vital signs," *IEEE Trans. Microw. Theory Techn.*, vol. 62, no. 6, pp. 1387–1399, Jun. 2014.
[36] M. Mercuri et al., "Enabling robust radar-based localization and vital signs monitoring in multipath propagation environments," *IEEE Trans. Biomed. Eng.*, vol. 68, no. 11, pp. 3228–3240, Nov. 2021.
[37] S. Pisa et al., "Comparison between delay and sum and range migration algorithms for image reconstruction in through-the-wall radar imaging systems," *IEEE J. Electromagn., RF, Microw. Med. Biol.*, vol. 2, no. 4, pp. 270–276, Dec. 2018.
[38] G. Sacco et al., "A radar system for indoor human localization and breath monitoring," in *2018 IEEE Int. Symp. Med. Meas. Appl.*, Aug. 2018, pp. 1–6.
[39] M. Mercuri et al., "Reconfigurable intelligent surface-aided indoor radar monitoring: A feasibility study," *IEEE J. Electromagn., RF, Microw. Med. Biol.*, vol. 7, no. 4, pp. 354–364, Dec. 2023.
[40] C. Feng et al., "Multitarget vital signs measurement with chest motion imaging based on MIMO radar," *IEEE Trans. Microw. Theory Techn.*, vol. 69, no. 11, pp. 4735–4747, Nov. 2021.
[41] T. Koda et al., "Noncontact respiratory measurement for multiple people at arbitrary locations using array radar and respiratory-space clustering," *IEEE Access*, vol. 9, pp. 106895–106906, 2021.
[42] Z. Xu et al., "Simultaneous monitoring of multiple people's vital sign leveraging a single phased-MIMO radar," *IEEE J. Electromagn., RF, Microw. Med. Biol.*, vol. 6, no. 3, pp. 311–320, Sep. 2022.
[43] M. Mercuri et al., "Automatic radar-based 2-D localization exploiting vital signs signatures," *Sci. Rep.*, vol. 12, pp. 1–11, May 2022.
[44] S. Wang et al., "A novel ultra-wideband 80 GHz FMCW radar system for contactless monitoring of vital signs," in *2015 37th Annu. Int. Conf. IEEE Eng. Med. Biol. Soc.*, Aug. 2015, pp. 4978–4981.
[45] R. Feger et al., "A 77-GHz FMCW MIMO radar based on an SiGe single-chip transceiver," *IEEE Trans. Microw. Theory Techn.*, vol. 57, no. 5, pp. 10020–1035, May 2009.
[46] L. Huang et al., "An implementation scheme of range and angular measurements for FMCW MIMO radar via sparse spectrum fitting," *Electronics*, vol. 9, no. 389, pp. 1–15, Feb. 2020.
[47] X. Wang et al., "A sparse representation scheme for angle estimation in monostatic MIMO radar," *Signal Process.*, vol. 104, pp. 258–263, Nov. 2014.
[48] P.-H. Juan, C.-Y. Chueh, and F.-K. Wang, "Distributed MIMO CW radar for locating multiple people and detecting their vital signs," *IEEE Trans. Microw. Theory Techn.*, vol. 71, no. 3, pp. 1312–1325, Mar. 2023.
[49] T. K. V. Dai et al., "Enhancement of remote vital sign monitoring detection accuracy using multiple-input multiple-output 77 GHz FMCW radar," *IEEE J. Electromagn., RF, Microw. Med. Biol.*, vol. 6, no. 1, pp. 111–122, Mar. 2022.
[50] G. Sacco and S. Pisa, "A MIMO radar for vital signs recording," in *2019 Photon. Electromagn. Res. Symp. - Spring*, Jun. 2019, pp. 387–393.
[51] Z. Fang et al., "Wide field-of-view locating and multimodal vital sign monitoring based on X-band CMOS-Integrated phased-array radar sensor," *IEEE Trans. Microw. Theory Techn.*, vol. 68, no. 9, pp. 4054–4065, Sep. 2020.
[52] F. Wang et al., "ViMo: Multi-person vital sign monitoring using commodity millimeter wave radio," *IEEE Internet Things J.*, vol. 8, no. 3, pp. 1294–1307, Feb. 2021.
[53] J. Xiong et al., "Vital signs detection with difference beamforming and orthogonal projection filter based on SIMO-FMCW radar," *IEEE Trans. Microw. Theory Techn.*, vol. 71, no. 1, pp. 83–92, Jan. 2023.
[54] G. Wang et al., "A hybrid FMCW-Interferometry radar for indoor precise positioning and versatile life activity monitoring," *IEEE Trans. Microw. Theory Techn.*, vol. 62, no. 11, pp. 2812–2822, Nov. 2014.
[55] M. Mercuri et al., "2-D localization, angular separation and vital signs monitoring using a SISO FMCW radar for smart long-term health monitoring environments," *IEEE Internet Things J.*, vol. 8, no. 14, pp. 11065–11077, Jul. 2021.
[56] G. Sacco et al., "A SISO FMCW radar based on inherently frequency scanning antennas for 2-D indoor tracking of multiple subjects," *Sci. Rep.*, vol. 13, no. 1, pp. 1–12, Oct. 2023.
[57] B. K. Park et al., "Arctangent demodulation with DC offset compensation in quadrature Doppler radar receiver systems," *IEEE Trans. Microw. Theory Techn.*, vol. 55, no. 5, pp. 1073–1079, May 2007.
[58] C. Li and J. Lin, "Random body movement cancellation in doppler radar vital sign detection," *IEEE Trans. Microw. Theory Techn.*, vol. 56, no. 12, pp. 3143–3152, Dec. 2008.
[59] M. Mercuri et al., "Analysis of signal processing methods to reject the DC offset contribution of static reflectors in FMCW radar-based vital signs monitoring," *Sensors*, vol. 22, no. 24, pp. 1–15, Dec. 2022.
[60] A. Bhattacharya and R. Vaughan, "Deep learning radar design for breathing and fall detection," *IEEE Sensors J.*, vol. 20, no. 9, pp. 5072–5085, May 2020.
[61] A. Hommes et al., "A fast tracking 60 GHz radar using a frequency scanning antenna," in *2014 39th Int. Conf. Infrared, Millimeter, Terahertz Waves*, Sep. 2014, pp. 1–2.
[62] A. Shoykhetbrod et al., "Concept for a fast tracking 60 GHz 3D-radar using frequency scanning antennas," in *2016 41st Int. Conf. Infrared, Millimeter, Terahertz Waves*, Sep. 2016, pp. 1–3.
[63] T. Geibig et al., "Compact 3D imaging radar based on FMCW driven frequency-scanning antennas," in *2016 IEEE Radar Conf.*, May 2016, pp. 1–5.
[64] A. Orth et al., "A novel approach for a MIMO FMCW radar system with frequency steered antennas for 3D target localization," in *2019 16th Eur. Radar Conf.*, Oct. 2019, pp. 37–40.
[65] Y. Alvarez-Lopez et al., "Frequency scanning based radar system," *Prog. Electromagn. Res.*, vol. 132, pp. 275–296, Jan. 2012.
[66] G. Sacco et al., "Analysis and modelling of rampart line antennas," *IET Microw., Antennas Propag.*, vol. 15, no. 12, pp. 1605–1617, Jul. 2021.
[67] W. C. Jakes and D. C. Cox, *Microwave Mobile Communications*. Hoboken, NJ, USA: Wiley-IEEE Press, 1994.
[68] J. D. Taylor, *Ultra-Wideband Radar Technology*. Boca Raton, FL, USA: CRC Press, 2001.
[69] M. Weenk et al., "A smart all-in-one device to measure vital signs in admitted patients," *PloS*, vol. 13, pp. 1–12, Feb. 2018.
[70] *Cardiac Monitors, Heart Rate Meters, Alarms*, ANSI/AAMI EC13-2002, Association for the Advancement of Medical Instrumentation.
[71] A. C. Morgado et al., "A chest patch for continuous vital sign monitoring: Clinical validation study during movement and controlled hypoxia," *J. Med. Internet Res.*, vol. 23, no. 9, Sep. 2021, Art. no. e27547.

Open Access provided by 'Univ Mediterranea di Reggio Calabria' within the CRUI CARE Agreement